

Modification of near-wall coherent structures by inertial particles

David H. Richter and Peter P. Sullivan

Citation: *Physics of Fluids* (1994-present) **26**, 103304 (2014); doi: 10.1063/1.4900583

View online: <http://dx.doi.org/10.1063/1.4900583>

View Table of Contents: <http://scitation.aip.org/content/aip/journal/pof2/26/10?ver=pdfcov>

Published by the [AIP Publishing](#)

Articles you may be interested in

[Large eddy simulations of Taylor-Couette-Poiseuille flows in a narrow-gap system](#)

Phys. Fluids **26**, 105108 (2014); 10.1063/1.4899196

[A hybrid stochastic-deconvolution model for large-eddy simulation of particle-laden flow](#)

Phys. Fluids **25**, 123302 (2013); 10.1063/1.4849536

[A unified probability density function formulation to model turbulence modification in two-phase flow](#)

Phys. Fluids **21**, 105101 (2009); 10.1063/1.3231831

[Stochastic simulation of Lagrangian trajectories in near-wall turbulence](#)

Phys. Fluids **18**, 075107 (2006); 10.1063/1.2236303

[Characterization of near-wall turbulence in terms of equilibrium and “bursting” solutions](#)

Phys. Fluids **17**, 015105 (2005); 10.1063/1.1825451

A horizontal banner with an orange-to-yellow gradient background. At the top center, the text '2014 Special Topics' is written in a large, white, sans-serif font. Below this text are five circular icons, each containing a different material structure and a label: 'PEROVSKITES' (red and black lattice), '2D MATERIALS' (red and black lattice), 'MESOPOROUS MATERIALS' (green and black porous structure), 'BIOMATERIALS/ BIOELECTRONICS' (yellow and black porous structure), and 'METAL-ORGANIC FRAMEWORK MATERIALS' (brown porous structure). At the bottom left, the 'AIP | APL Materials' logo is displayed. At the bottom right, a red ribbon contains the text 'Submit Today!' in white.

Modification of near-wall coherent structures by inertial particles

David H. Richter¹ and Peter P. Sullivan²

¹*Department of Civil and Environmental Engineering and Earth Sciences,
University of Notre Dame, Notre Dame, Indiana 46556, USA*

²*National Center for Atmospheric Research, P.O. Box 3000, Boulder, Colorado 80307, USA*

(Received 27 February 2014; accepted 16 October 2014; published online 30 October 2014)

Direct numerical simulations are combined with two-way coupled Lagrangian point particles to study the effect of Reynolds number on particle-turbulence interaction. Turbulent planar Couette flow is simulated at a constant dispersed phase mass loading of $\phi_m = 0.25$ for particle Stokes numbers of $St_K = [O(1), O(10), O(100)]$ (based on the Stokes time scale of the particle and the Kolmogorov time scale of the flow) and bulk Reynolds numbers of $Re_b = [8100, 24000, 72000]$ (based on the plate velocity difference and separation distance). Statistics of swirling strength $|\lambda_{ci}|$ are used to evaluate the impact of particles on near-wall motions which are responsible for turbulent, wall-normal momentum transport. Instantaneously, the number of high-strength swirling motions near the wall decreases significantly in the presence of particles, and this trend is enhanced with increasing Re_b . Conditional averages are computed using linear stochastic estimation, providing the average structures responsible for ejection events near the wall. These conditional eddies are weakened substantially by the presence of the dispersed phase, and this effect is again enhanced with increasing Re_b . We propose a mechanism where particles, by interfering with the hairpin regeneration process near the wall, can influence turbulent fluxes in a way that increases with Re_b despite only having direct interaction with scales on the same order as their small physical size. At the same time, turbulent momentum flux concentrated at higher wavenumbers with increasing Re_b allows small particles to be effective agents for altering turbulent transport. © 2014 AIP Publishing LLC. [<http://dx.doi.org/10.1063/1.4900583>]

I. INTRODUCTION

Particle-turbulence interaction is a topic which has garnered continual attention for many years in areas ranging from industrial pneumatic transport¹ to geophysical flows.^{2,3} We approach this subject broadly motivated by sea spray suspended within the marine atmospheric boundary layer, but for this study we are specifically interested in the ability of a dispersed phase to alter turbulent momentum^{4,5} and heat⁶ fluxes in wall-bounded flows. Richter and Sullivan⁴ demonstrate that inertial particles damp Reynolds shear stresses in turbulent planar Couette flow, the magnitude of this reduction depending on the particle Stokes number, and show that this is tightly linked to the modification of near-wall vortical structures. The goal of the current study is to more thoroughly explore the connection between the dispersed phase and near-wall coherent motions, and characterize how this changes with increasing Reynolds number through an idealized set of simulations.

Many studies have investigated turbulence modification in particle-laden, wall-bounded flows,⁷⁻¹⁰ but only a subset focus on modifications to the turbulent Reynolds stresses. Owen¹ attempts to review and explain pressure drop measurements of various particle-laden pipe flow experiments, and notes in passing that the measured skin friction in a pipe can appear to be reduced by the dispersed phase, but that this simply represents a transition between momentum flux carried by the air and that carried by the particles. Rashidi *et al.*¹¹ show that large particles (1100 μm) increase the frequency of wall ejection events in a turbulent boundary layer, consequently increasing the

turbulent wall-normal momentum flux, while small particles ($120\ \mu\text{m}$) exhibit an opposite behavior, reducing the number of ejections events and thus the Reynolds stresses. They note that each of these effects is enhanced with increased particle concentration, and describe a physical process where particles accumulate in low-speed streaks and are carried upwards with the low-speed fluid during ejection events.

Righetti and Romano¹² performed experiments in a horizontal, open-channel flow at $Re \approx 15\,000$ and were able to measure turbulent properties very close to the bottom boundary. They find that in this setup, where particles settle towards the bottom wall due to gravity, the dispersed phase reduces velocity fluctuations and Reynolds shear stresses in the carrier phase, but only at sufficiently large distances from the wall ($z^+ \geq 10$, where “+” refers to scaling with viscous wall units). Very close to the wall ($z^+ < 10$), Reynolds stresses are enhanced, and the crossover point is attributed to momentum being exchanged between the two phases at near-wall ejection locations. They perform a quadrant analysis and show that for $z^+ \geq 10$, the reduction in Reynolds stress comes from a suppression of both ejection and sweep events (quadrants 2 and 4 in the $u'-w'$ plane), with a larger reduction in the ejection strengths. They also compute time-weighted contributions from each quadrant and show that the relative contribution from “coherent” motions to the total Reynolds stress (quadrants 2 and 4) is substantially reduced relative to the “incoherent” motions (quadrants 1 and 3) for $z^+ \geq 10$.

Meanwhile, two-way coupled numerical simulations have provided significant insight into the details of momentum exchange and subsequent turbulence modification in particle-laden turbulent flows which experimental studies are unable to directly observe.^{13,14} In the context of wall-bounded flows, simulations with small, heavy particles, such as those performed by Li *et al.*¹⁰ and Zhao *et al.*,¹⁵ generally exhibit reductions of the turbulent Reynolds stress. Mito and Hanratty¹⁶ show, for a turbulent channel with surface entrainment/deposition (i.e., particles are adsorbed to and ejected from the surface), that the momentum carried by the dispersed phase becomes a significant fraction of the total stress at the expense of the carrier phase Reynolds stress. This would imply a reduction of carrier phase turbulent fluxes due to the reduction of near-wall vortical activity. Similarly, Vreman¹⁷ uses numerical simulations to study particle-laden pipe flow, and shows that at very large mass loadings, the carrier phase turbulent flux can be nearly eliminated and that all momentum transfer is taken up by the dispersed phase. Furthermore, he shows that even with moderate mass loadings, the Reynolds shear stress of the dispersed phase can be equal in magnitude to that of the carrier phase, in agreement with the experiments of Caraman *et al.*¹⁸ and Borée and Caraman.¹⁹

Further highlighting the mechanistic insight which can be provided by two-way coupled simulations, the conditional averages computed by Dritselis and Vlachos^{20,21} show that near-wall, quasi-streamwise vortices are weakened and enlarged by the dispersed phase in a vertical channel. A weakening of these motions, which is one of the emphases of the current study, provides a more thorough understanding of Reynolds shear stress modifications near the wall. To this end, Zhao *et al.*²² compute interphasial energy budgets between particles and the carrier phase in turbulent channel flow to demonstrate extra energy dissipation due to the presence of inertial particles as well as their ability to redistribute energy both directionally and spatially. Reductions in the wall-normal Reynolds shear stress, which is highly dependent on particle inertia, is found to result from the correlations of fluctuating particle forces with fluctuating carrier phase velocities.

It is clear that the dispersed and carrier phases exchange momentum and modify carrier phase Reynolds shear stresses in wall-bounded turbulence, but it is not clear that the total momentum flux remains constant. That is, does the combined wall-normal momentum transport from both phases remain constant in these flows, and how does this change with increasing scale separation (i.e., Reynolds number)? More generally, how does the two-way coupling of small, heavy particles in a turbulent wall-bounded flow change as the flow Reynolds number becomes asymptotically large? This has direct relevance to many geophysical and industrial applications where flow length and/or velocity scales can be very large while the dispersed phase remains small. We attempt to answer these questions using an idealized formulation, which utilizes direct numerical simulations of planar Couette flow two-way coupled with Lagrangian point-particles. We focus particularly on turbulent near-wall structures and how their interactions with inertial particles change with increasing Reynolds number, since only by understanding the effects of Reynolds number can we hope to predict effects

at very large (i.e., geophysical) scales. It is important to note that owing to the simplified nature of the point-particle approximation, conclusions drawn from the current analysis are only valid for physical systems which meet the underlying conditions (small, heavy particles at low volume concentrations), and one must take great care extrapolating results to systems which lie beyond this range of validity. Under certain conditions, such as when particles exceed the Kolmogorov scale of the flow, other numerical techniques, such as fully resolved dispersed phase simulations,²³ must be used instead.

II. PROBLEM FORMULATION

A. Governing equations

For this work, the standard Lagrangian point-particle approximation is used in conjunction with direct numerical simulation (DNS) of the carrier phase. To represent the motion of a particle with a density ρ_p much greater than that of the surrounding carrier phase fluid, $\rho_p/\rho_f \gg 1$, and a diameter d_p smaller than the smallest scales of the turbulent flow, $d_p/\eta_K \ll 1$ where η_K is the Kolmogorov length scale, a simple force balance yields equations for the particle position $x_{p,i}$ and velocity $v_{p,i}$:

$$\frac{dx_{p,i}}{dt} = v_{p,i}, \quad (1)$$

$$\frac{dv_{p,i}}{dt} = \frac{f_i}{m_p} = (1 + 0.15Re_p^{0.687}) \frac{1}{\tau_p} (u_{f,i} - v_{p,i}), \quad (2)$$

where m_p is the particle mass and f_i is the force acting on the particle. $\tau_p = \rho_p d_p^2 / 18\mu_f$ is the particle Stokes relaxation time, where μ_f is the dynamic viscosity of the carrier phase fluid. The particle Reynolds number, $Re_p = |u_{f,i} - v_{p,i}|d_p/\nu_f$, is defined based on the difference between the local fluid velocity $u_{f,i}$ interpolated to the particle location using sixth-order Lagrange interpolation (modified at the wall to provide symmetric interpolation stencils in the vertical direction) and the particle velocity. Equation (2) includes an empirical Reynolds number correction to the Stokes drag over a solid sphere.²⁴ By assuming that $\rho_p/\rho_f \gg 1$ and that $d_p/\eta_K \ll 1$, it follows that Re_p is likely small as well, which taken together imply that particle wake effects and distortions to the local velocity field are small. Furthermore, other terms in the equation of motion of a solid sphere²⁵ such as the Basset history force and Faxén corrections are assumed negligible.

The carrier phase is solved using the incompressible Navier-Stokes equations:

$$\frac{\partial u_j}{\partial x_j} = 0, \quad (3)$$

$$\frac{\partial u_i}{\partial t} + u_j \frac{\partial u_i}{\partial x_j} = -\frac{1}{\rho_f} \frac{\partial p}{\partial x_i} + \nu_f \frac{\partial^2 u_i}{\partial x_j \partial x_j} + \frac{1}{\rho_f} F_i. \quad (4)$$

In this study, we are particularly concerned with the effect of particles on the surrounding turbulent flow; their feedback onto the carrier phase is represented through F_i , a two-way coupling force. Similar to other studies,^{26,27} F_i is computed by projecting the force exerted from each individual particle ($-f_i$ from Eq. (2)) onto the nodes of the surrounding carrier phase computational mesh; see Richter and Sullivan⁴ for additional details.

B. Numerical implementation

Turbulent plane Couette flow develops between two infinitely parallel plates moving with equal and opposite velocity $U_0/2$. It is well-known^{28,29} that large, quasi-coherent, streamwise structures develop in this flow (hereafter referred to as rollers) which span the entire distance H between the plates, have a spanwise wavelength of approximately $2H$, and extend upwards of $15H$ in the streamwise direction. These rollers are turbulent in nature and exist simultaneously with the more commonly recognized quasi-streamwise vortices and hairpins of wall-bounded turbulence. As a

result their removal (e.g., via a triple Reynolds decomposition) is not straightforward since they behave as an inherent part of the overall flow.

In the context of DNS, large spanwise and streamwise domain extents are required to fully capture the rollers and obtain resolved statistics.^{28,29} In the present case, however, computational constraints limit the domain to dimensions of $[2\pi H, 2\pi H, H]$. The present use of periodic boundary conditions in the streamwise (x) and spanwise (y) directions therefore approximates these structures as infinitely long (since they span the entire length of the domain) with a spanwise wavelength slightly modified by spanwise confinement. Preliminary tests indicate that while certain quantities such as two-point correlations are sensitive to a restricted domain size, the statistics of interest to this study (e.g., the Reynolds stress) are not strongly influenced by spanwise or streamwise extent, in agreement with the findings of Tsukahara *et al.*²⁹ Furthermore, the aim of this study is to describe the general role of inertial particles in vertical momentum transport within wall-bounded, turbulent flows, and not to focus on Couette flow specifically. For this reason, the infinite span of the midplane structures does not change our basic findings, and we regard the comparison of laden and unladen planar Couette flows in this truncated domain as fully adequate for our purposes.

A pseudospectral method is employed in the periodic directions (x and y), and second-order finite differences are used for spatial discretization in the inhomogeneous, wall-normal z direction. A low-storage, third-order Runge-Kutta (RK3) scheme is used to discretize the time domain.³⁰ Incompressibility is enforced by solving a pressure Poisson equation to guarantee a divergence-free velocity field at each RK stage. At the solid walls, the particles bounce elastically and no-slip is enforced on the carrier phase. In terms of the centerline Kolmogorov length scale η_K , the coarsest horizontal grid resolution among all cases is $[\Delta x/\eta_K, \Delta y/\eta_K] = [4.88, 2.44]$. The vertical grid is stretched across the height, and in terms of the viscous length, Δz_{wall}^+ (the spacing at the wall normalized with viscous wall units) varies between 0.65 and 1.2 across all cases.

Additional details regarding the numerical method and code can be found in our previous work.⁴ In all simulations, the carrier phase velocity fields are initialized by a previously obtained unladen case, while the particles are randomly and homogeneously distributed throughout the domain with zero initial velocity. Statistics are obtained from horizontal and temporal averaging over a time of at least $tU_0/H = 4000$.

C. Simulation parameters

The overall goal of this study is to use a simplified numerical formulation to study fundamental questions regarding wall-normal momentum transport in the presence of small inertial particles. In order to both achieve large Reynolds numbers given limited computational resources as well as simplify the physical system to the most basic particle-turbulence interactions, the simulations performed in this study use the non-interacting point-particle approximation in the absence of gravity. This fundamental understanding is critical for the large-scale prediction and modeling of surface stresses in many geophysical and industrial systems. From the relatively simple numerical implementation used presently, additional processes will be added one-by-one in the future to provide a full physical understanding of each. The current work is therefore a first step in a larger process to form a deep understanding which can be used to develop reliable parameterizations for large-scale, two-way coupled modeling efforts.

By utilizing turbulent plane Couette flow, as opposed to the more common turbulent channel flow, the simulations represent a system where wall-normal momentum transport is dominated by the same ejection and sweep processes which occur in turbulent channels or boundary layers (to be illustrated subsequently), but where the presence of rollers provides a unique length- and timescale with which the particles can interact in addition to those provided by the near-wall turbulence. Furthermore, the use of plane Couette flow provides a convenient framework for quantitatively and unambiguously comparing momentum flux components since the total vertical momentum flux is constant with height. Since we are ultimately not concerned with Couette flow specifically, but rather the general interaction of shear-generated wall turbulence and small, heavy particles, the current objective is to formulate a mechanistic understanding of the role of a dispersed phase on near-wall

coherent structures and momentum transport, as well as how this changes with increasing Reynolds number.

The parameters of interest in this study are the particle Stokes number, defined as the ratio of the particle acceleration timescale to the Kolmogorov timescale at the channel centerline ($St_K = \tau_p/\tau_K$), the particle mass concentration ϕ_m , defined as the ratio of the total particle mass in the domain to the carrier phase mass, and the bulk Reynolds number $Re_b = HU_0/\nu_f$. It should be noted that τ_K varies by a factor of roughly 5 between the centerline and wall in all cases.

By making the non-interacting point-particle approximation, we restrict comparison of the simulation results to physical systems which meet the following conditions: (1) the particle diameters are smaller than the smallest turbulence scales, (2) the particle Reynolds number remains small, thus ensuring negligible distortion to the surrounding flow field, and (3) the volume fraction remains small to ensure a low influence of particle-particle collisions. Furthermore, upon nondimensionalizing the system of equations, the dimensional quantities ρ_p and d_p do not appear independently (except indirectly, since d_p is used to compute Re_p and determines the elastic collision distance at the wall). Therefore, we choose to maintain a constant d_p across all cases with the purpose of maintaining an equal rebound distance at the wall. As demonstrated in Richter and Sullivan,⁴ if one were to change d_p between cases, the ability of particles to become stuck in the viscous sublayer changes between cases, which modifies the number of particles in the bulk of the channel and thus indirectly influences the turbulence modification and makes comparisons between cases ambiguous. In the present model, this process of particles becoming stuck at the wall is exaggerated due to the lack of a lifting force on the particle.

For all cases, therefore, we set $d_p = 200 \mu\text{m}$ (if the channel units are in m), which provides $d_p^+ \approx 1$ for all cases—sufficient for re-suspension into the bulk of the domain³¹ and well under the Hinze estimate for maximum stable droplet diameter³² given the computed dissipation rate. With d_p set in this way, ρ_p is used as a free parameter to determine the particle Stokes number. Note that these simulations are nearly equivalent to setting $\rho_p = 1000$ (e.g., water in air) and changing d_p and N_p (the number of particles) to maintain the same St_K and ϕ_m , while artificially forcing the particles to collide with the wall at $100 \mu\text{m}$ instead of their radius. The only differences in this system would be due to the empirical correction of Eq. (2), and tests have shown that this is minimal in terms of the quantities discussed subsequently (Reynolds stresses, spectra, conditional averages). Thus, in accordance with the point-particle approximation, the particle size is somewhat arbitrary and only the dimensionless particle characteristics are considered.

Simulations at constant mass loading $\phi_m = 0.25$ are performed for $St_K = [O(1), O(10), O(100)]$ at three increasing bulk Reynolds numbers: $Re_b = [8100, 24000, 72000]$. This corresponds to friction Reynolds numbers of $Re_\tau \equiv Hu_\tau/2\nu_f \approx [120, 320, 900]$, where u_τ is the friction velocity defined using the wall stress τ_w : $u_\tau = \sqrt{\tau_w/\rho_f}$. These and other parameters are included in Table I. The Reynolds number is increased by successively doubling the domain height H while simultaneously increasing U_0 such that the Kolmogorov length scale at the channel centerline remains roughly constant (in dimensional units). Since η_K is computed *a posteriori*, its value varies slightly between cases.

Finally, other simulation-based studies^{10,33} have shown that particle collisions can have a significant impact on particle fluctuation statistics and, in two-way coupled simulations, on carrier phase turbulence statistics as well. The current particle model, however, does not incorporate particle collisions for the following reasons. As mentioned previously, our work is broadly motivated by a fluid system involving water droplets in air. These droplets do not experience elastic collisions as implemented in typical collision kernels, but instead undergo coalescence and breakup during particle-particle interactions. Given the uncertainty involved with existing droplet coalescence/breakup models, as well as the computational effort required for large particle numbers, we have opted to allow particles to occasionally overlap in space based on our choice of d_p . In certain regions within the flow this may perhaps lead to artificially high mass concentrations, but in the context of water droplets may actually provide a crude approximation of the coalescence process.

The choices of ρ_p , d_p , and N_p outlined in Table I result in a maximum bulk particle volume fraction of $\phi_V = 2.5e - 3$, where it is reasonable to expect a low influence of particle collisions. Indeed, by using standard kinetic theory, we have estimated that in worst-case conditions (run 10 near

TABLE I. Summary of simulation parameters: Bulk Reynolds number $Re_b = HU_0/\nu_f$; friction Reynolds number $Re_\tau = Hu_\tau/2\nu_f$; grid resolution as number of grid points in each direction ($N_x \times N_y \times N_z$); bulk particle mass loading ϕ_m ; bulk particle volume fraction ϕ_V (ratio of total dispersed phase volume to carrier phase volume); particle Stokes number St_K ; particle Stokes number based on wall units St^+ ; ratio of particle density to fluid density ρ_p/ρ_f ; particle diameter normalized by Kolmogorov length d_p/η_K ; particle diameter normalized by viscous wall units d_p^+ ; number of particles N_p ; and Kolmogorov timescale at $z^+ = 50$ normalized by the unladen value.

Run	Re_b	Re_τ	$N_x \times N_y \times N_z$	ϕ_m	ϕ_V	St_K	St^+	ρ_p/ρ_f	d_p/η_K	d_p^+	N_p	$\frac{\tau_K}{\tau_{K,un}} _{z^+=50}$
1	8100	121	$128 \times 256 \times 128$	0.0	0.0						0	1
2	8100	122	$128 \times 256 \times 128$	0.25	2.5×10^{-3}	1.2	8.2	100	0.46	1.2	1.5×10^6	1.14
3	8100	124	$128 \times 256 \times 128$	0.25	2.5×10^{-4}	12	85	1000	0.46	1.2	1.5×10^5	1.09
4	8100	122	$128 \times 256 \times 128$	0.25	3.1×10^{-5}	97	656	8000	0.47	1.2	1.9×10^4	1.07
5	24000	325	$256 \times 512 \times 256$	0.0	0.0						0	1
6	24000	317	$256 \times 512 \times 256$	0.25	2.5×10^{-3}	1.1	14	100	0.45	1.6	1.2×10^7	1.24
7	24000	331	$256 \times 512 \times 256$	0.25	2.5×10^{-4}	9.5	152	1000	0.41	1.7	1.2×10^6	1.14
8	24000	321	$256 \times 512 \times 256$	0.25	3.1×10^{-5}	94	1146	8000	0.46	1.6	1.5×10^5	1.08
9	72000	917	$512 \times 1024 \times 512$	0.0	0.0						0	1
10	72000	848	$512 \times 1024 \times 512$	0.25	2.5×10^{-3}	1.1	25	100	0.45	2.1	9.6×10^7	1.47
11	72000	869	$512 \times 1024 \times 512$	0.25	2.5×10^{-4}	9.8	262	1000	0.42	2.2	9.6×10^6	1.33
12	72000	911	$512 \times 1024 \times 512$	0.25	3.1×10^{-5}	83	2307	8000	0.43	2.3	1.2×10^6	1.07

the walls), the mean volume concentrations which develop would lead to an average time between collisions on the order $10\tau_p$. Thus, even in the regions of highest concentrations, the particles on average can accelerate to the local velocity before a collision would have occurred, indicating that two-way coupling effects may be similar to cases where particle-particle collisions are included. As noted above, however, any potential violation of the non-interacting assumption can be avoided within the point-particle framework by merely making d_p smaller, enforcing a uniform collision distance at the wall, and adjusting ρ_p and N_p to maintain the mass fraction and Stokes numbers of interest. This test has been performed for run 2 specifically where St_K and ϕ_m are matched but while choosing ρ_p and d_p in a way that results in a volume fraction of $\phi_V = 3.1e - 5$, and this provides nearly identical results as the original case. Overall, therefore, the results presented herein are thus generally applicable to any system where small, non-interacting particles are influencing wall-bounded turbulent flow, as long as the particle Stokes number and mass fraction are similar.

III. MOMENTUM FLUX

The mean horizontal momentum budget is derived by taking a horizontal average of Eq. (4):

$$\rho_f \nu_f \frac{\partial^2 \langle U \rangle}{\partial z^2} - \rho_f \frac{\partial}{\partial z} \langle u'w' \rangle + \langle F_x \rangle = 0. \quad (5)$$

Throughout, averaging is denoted with $\langle \cdot \rangle$ and fluctuating quantities are indicated as $[\cdot]'$. As noted previously, F_x refers to the horizontal feedback force resulting from the dispersed phase. For plane Couette flow, one can define a total stress which is constant across the channel height:

$$\tau(z) = \tau_w = -\rho_f \langle u'w' \rangle + \rho_f \nu_f \frac{\partial \langle U \rangle}{\partial z} + \int_0^z \langle F_x(z^*) \rangle dz^*, \quad (6)$$

where, as defined previously, τ_w is the stress at the wall. The total stress includes (in the order of terms on the right hand side of Eq. (6)) the turbulent carrier phase flux which vanishes at the wall, the viscous stress, and an additional stress due to the dispersed phase momentum flux. This extra particle stress physically represents horizontal momentum being transferred in the wall-normal direction by the average motion of the particles. In our previous work,⁴ profiles of these stresses are presented and analyzed for $Re_b = 8100$. These profiles are presented in Figure 1(a), along with the profiles for the two additional Reynolds numbers in Figures 1(b) and 1(c). As a representative

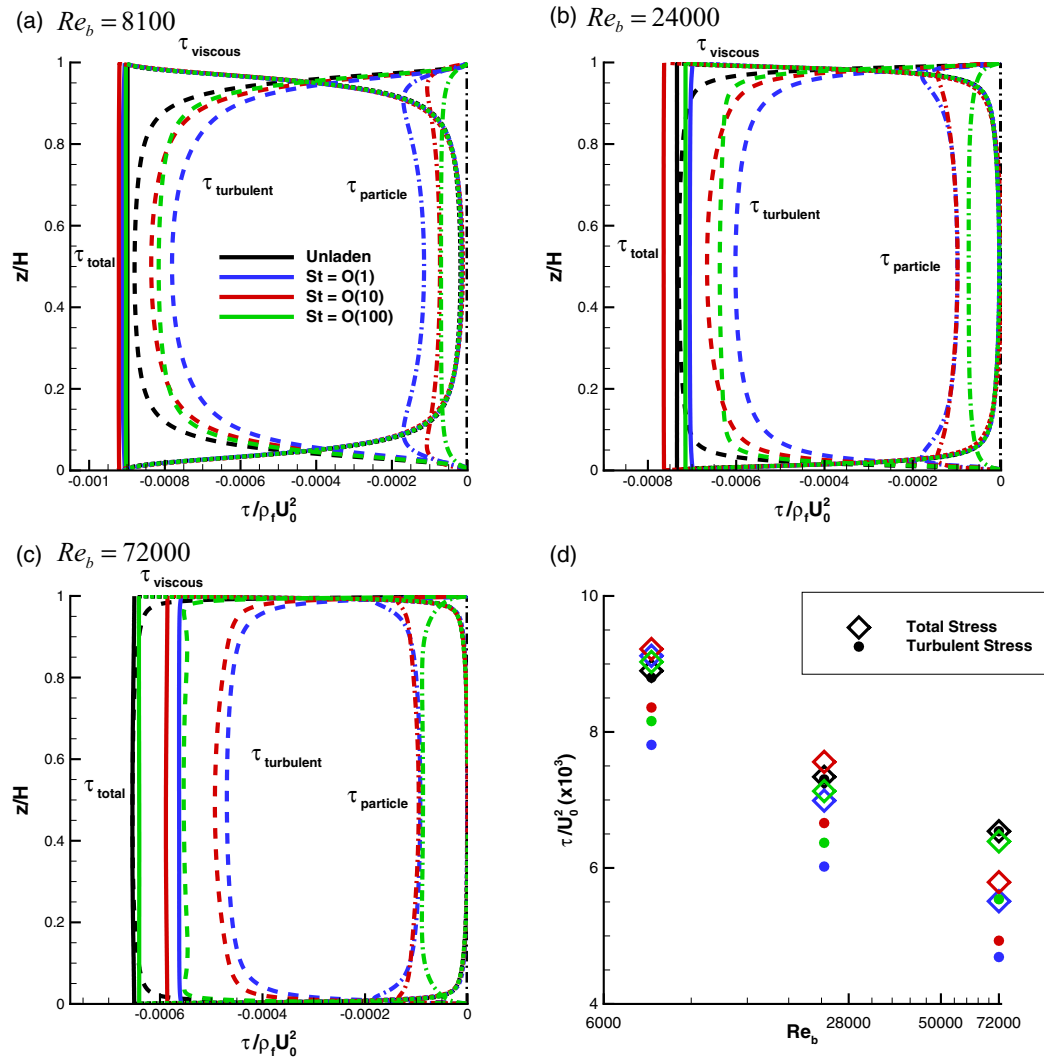


FIG. 1. (a)–(c) Profiles of the total (solid), turbulent (dashed), viscous (dotted), and particle (dotted-dashed) stresses over the channel height for each particle Stokes number. Stress normalized by $\rho_f U_0^2$ and z normalized by H . See legend for color designations. Note that the x axis changes scale. (d) Normalized turbulent flux $\tau_{turb}/\rho_f U_0^2 = -\langle u'w' \rangle / U_0^2$ and total flux $\tau_{total}/\rho_f U_0^2$ evaluated at $z = H/2$ as a function of Re_b . Hollow diamonds refer to the total flux and filled circles refer to the turbulent flux. Note that the abscissa is on a logarithmic scale.

measure of the turbulent flux modification, Figure 1(d) shows the normalized turbulent flux at the channel mid-height $\tau_{turb}(H/2)/\rho_f U_0^2 = -\langle u'w' \rangle_{H/2}/U_0^2$, along with the total flux, for all cases as a function of Re_b .

With increasing Reynolds number, the normalized turbulent stress at the centerline for the uncoupled cases decreases monotonically, which is consistent, for example, with the decrease of the skin friction coefficient of turbulent pipe flow or a turbulent boundary layer with increasing Reynolds number (see, e.g., Ref. 34). The addition of particles, in all cases, then reduces the unladen turbulent flux; in some cases by up to 30%. This reduction is largest for the $St_K = O(1)$ and least for either the $St_K = O(10)$ or $St_K = O(100)$ particles, depending on Re_b and vertical position. At the lower two Reynolds numbers, it appears that the centerline turbulent flux is reduced least for the $St_K = O(10)$ particles in Figure 1(d); however, this is not necessarily true when taking into consideration the slight increase in the total flux for $St_K = O(10)$. As will be shown elsewhere (e.g., Table I, last column), it is generally true that turbulence modification is maximized for $St_K = O(1)$ and decreases monotonically with increasing Stokes number, particularly near the walls.

Figure 1 indicates that the particles, over the entire range of Reynolds number probed, greatly inhibit the amount of horizontal momentum transported in the wall-normal direction by carrier phase turbulent motions, and that this reduction is offset (at least partially) by a rise in the particle stress. At the lowest Reynolds number, the total amount of wall-normal momentum transfer remains constant but partitioned between the flow turbulence and particle motion. With increasing Reynolds number, however, the momentum carried by the particles saturates and, accompanied by a continued reduction in the turbulent stress, the total stress decreases. This will be discussed in more detail in Sec. V.

Reductions in carrier phase Reynolds stress have been observed in numerous experimental^{11,12} and numerical^{10,16,17} studies. From the current simulations, as the Reynolds number increases this effect becomes more pronounced, as measured by the gap between the unladen and laden cases. Note that the minimal changes to the viscous flux indicate that the mean velocity profile experiences only minor modifications (except at the wall in certain cases). We will return to this figure in Sec. V.

It is worthwhile to note that Hadinoto *et al.*³⁵ perform vertically oriented pipe flow experiments to specifically probe the effect of Reynolds number on particle-laden turbulence modification. Holding the dispersed phase mass fraction constant, they find that the centerline difference between laden and unladen turbulent streamwise fluctuations widens with increasing Re for two different particle sizes. While their observed turbulence augmentation contrasts with the present turbulence suppression (this discrepancy is likely due to the differences in particle size relative to the Kolmogorov scales as well as the physical setup—gravity is acting in their streamwise direction), Hadinoto *et al.*³⁵ demonstrate that the turbulence modifications found at low Re can be amplified by solely increasing the bulk Reynolds number.

To better understand the mechanism through which particles modify the carrier phase turbulent flux (observed in Figure 1), it is instructive to first determine the length scales over which the particles exert their influence. All existing DNS studies of particle-laden turbulence (either homogeneous isotropic or wall-bounded) are restricted to relatively low Reynolds numbers, and as a result have a limited range of scales which can be resolved. Questions remain, therefore, on the scale range over which particles modify the energy spectrum. Kulick *et al.*,⁷ for instance, present energy spectra from turbulent channel flow experiments at $Re = 13\,800$ which show distinct frequency bands where the dispersed phase reduces energy content relative to the unladen case, while Tsuji *et al.*⁹ show spectral energy attenuation at low frequencies but energy enhancement at high frequencies in turbulent pipe flow with large ($\geq 200\ \mu\text{m}$) particles.

One of the goals of the current study, therefore, is to identify the degree to which particles under the point-particle approximation are “felt” by motions which exist on much larger time and length scales than the individual particles. To visualize this, shear stress cospectra $-E_{13}(\kappa_1)$ (i.e., the real part of the Fourier-transformed correlation $\langle u'w' \rangle$) multiplied by the streamwise wavenumber κ_1 at a height of $z^+ = 50$ are shown for increasing Reynolds numbers in Figure 2. Shear stress cospectra are plotted instead of streamwise energy spectra since we are ultimately concerned with wall-normal momentum transport and the motions which cause it. Note that integrating the profiles in Figure 2 yields the nondimensional turbulent flux $-\langle u'w' \rangle / U_0^2$ at $z^+ = 50$, and Figure 2 is plotted in a way so that areas are proportional to this flux, i.e., $\int \kappa_1 E_{13}(\kappa_1) d(\ln \kappa_1) = -\langle u'w' \rangle$.

The Couette rollers, which, as noted previously are numerically represented as infinitely long due to streamwise periodicity, are manifested as increases in $-E_{13}/U_0^2$ at the lowest wavenumbers. This is prominent at the low-wavenumber end of Figures 2(b) and 2(c). At higher wavenumbers, a maximum forms around $\kappa_1 H \approx 20$. Since the area under the curve is proportional to $-E_{13}/U_0^2$, the motions associated with this $\kappa_1 H \approx 20$ peak clearly contribute most to the total integrated Reynolds stress $\langle u'w' \rangle$. More importantly, the wavelengths associated with this peak correspond to the size of the conditional hairpins which will be discussed in Sec. IV B. For the case of $Re_b = 8100$, the $\kappa_1 H \approx 20$ peak overlaps with the contribution from the Couette rollers, while at high Re_b , it is the motions corresponding to the peak (i.e., the near-wall turbulence) and not the Couette rollers themselves which contribute most to the turbulent flux of momentum.

With the addition of particles, momentum flux almost universally decreases at all wavenumbers (the exceptions being at the lowest few wavenumbers where the strength of the rollers dominates). For $Re_b = 8100$ in Figure 2(a), the decrease in the cospectra is relatively small, particularly at high

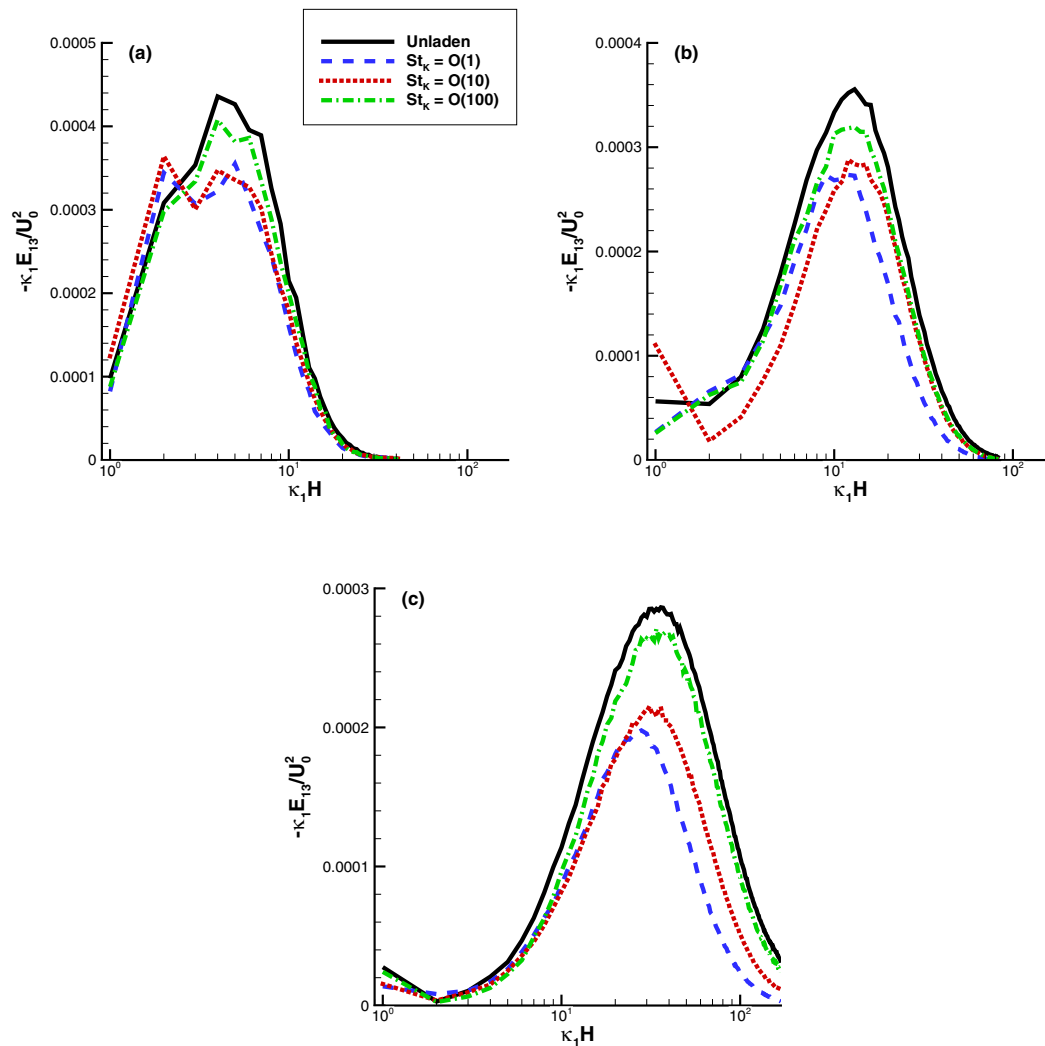


FIG. 2. Shear stress cospectra multiplied by the streamwise wavenumber, $-\kappa_1 E_{13}/U_0^2$, as a function of the normalized streamwise wavenumber $\kappa_1 H$ for (a) $Re_b = 8100$, (b) $Re_b = 24\,000$, and (c) $Re_b = 72\,000$. Cospectra taken at a height of $z^+ = 50$. See legend for line associations with particle Stokes number. Note that the ordinates differ in scale. Since the spectra are multiplied by κ_1 and the ordinate uses a linear scale, the area represents the contribution to $-\langle u'w' \rangle / U_0^2$.

$\kappa_1 H$, with the $St_K = O(1)$ particles producing the largest decrease. For $Re_b = 24\,000$ in Figure 2(b), the decrease in the cospectra is much more pronounced, again with $St_K = O(1)$ particles exhibiting the strongest effect for much of the range of $\kappa_1 H$. Finally at $Re_b = 72\,000$ in Figure 2(c), the energy content of the $\langle u'w' \rangle$ correlation is further damped by the presence of the dispersed phase.

No “crossover” wavenumber is found at high wavenumbers, above which energy content is augmented by the dispersed phase—behavior seen in a wide variety of experimental and numerical studies for one-dimensional energy spectra.^{17,36–38} Instead, Figure 2 indicates that particles under the point-particle approximation, depending on their inertia, inhibit turbulent motions across nearly the entire range of length and timescales (with the exception of the midplane rollers). This universal reduction in turbulent energy is in qualitative agreement with the two-way coupled channel flow simulations of Zhao *et al.*²² For the highest wavenumbers, this effect is maximized when $St_K = O(1)$, while below $\kappa_1 H \approx 10$ the $St_K = O(10)$ particles provide nearly the same (or larger) decrease. This dependence on St_K of the ranges of the cospectra which are most damped provides clear evidence that the particles tend to inhibit motions according to their own inertial timescale. This suggests that at even higher Reynolds numbers, the wavenumber bands of Kulick *et al.*⁷ may be observed.

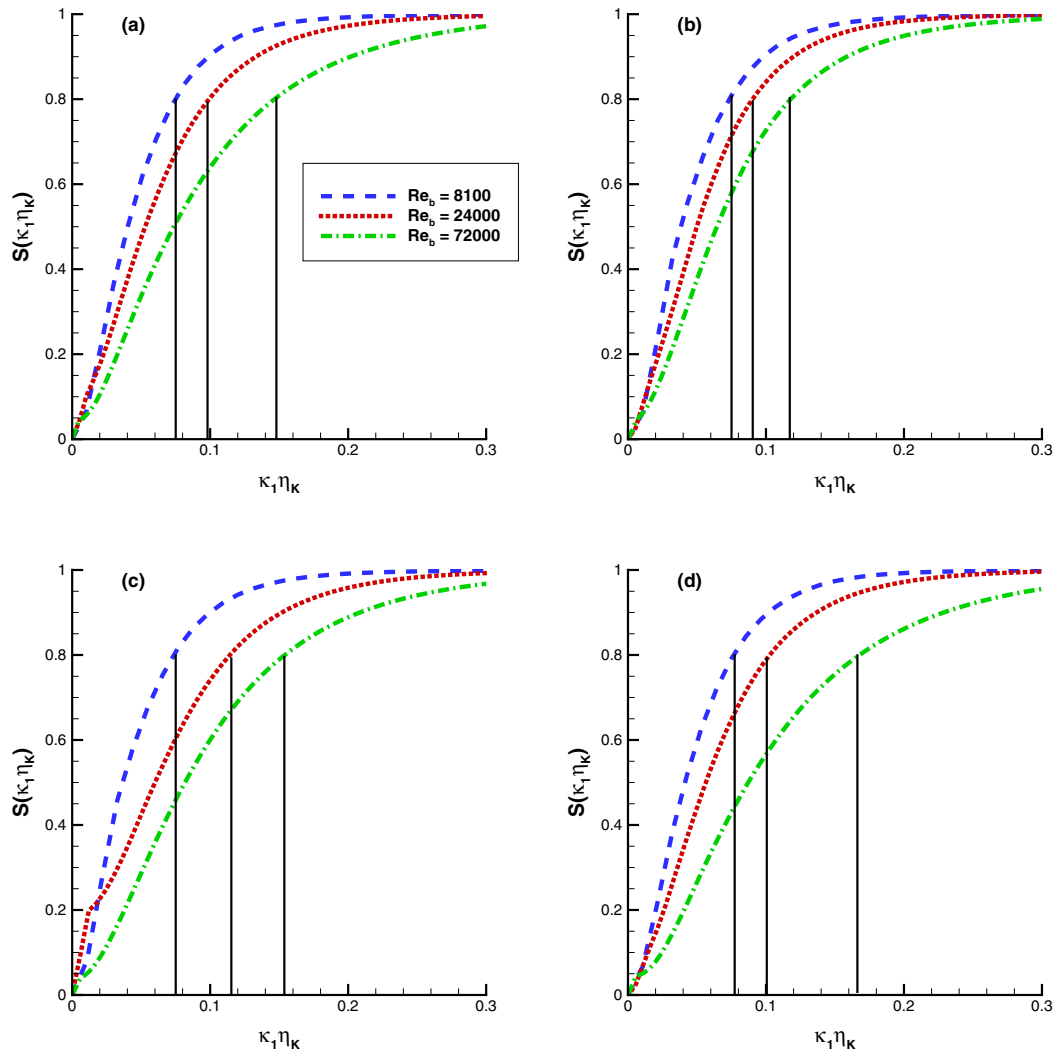


FIG. 3. Running cospectra integral given by Eq. (7) as a function of normalized streamwise wavenumber $\kappa_1 \eta_K$. (a) Unladen case; (b) $St_K = O(1)$ particles; (c) $St_K = O(10)$ particles; and (d) $St_K = O(100)$ particles. Vertical black lines show the wavenumber where the integral reaches 80% of the total turbulent flux $\langle u'w' \rangle$.

It is important to note that the momentum is being transferred by increasingly higher-wavenumber motions as Re_b is increasing. Defining the running integral of the shear stress cospectra as

$$S(\hat{\kappa}_1) = -\frac{1}{\langle u'w' \rangle} \int_0^{\hat{\kappa}_1} E_{13}(\hat{\kappa}_1^*) d\hat{\kappa}_1^*, \quad (7)$$

where the wavenumber $\hat{\kappa}_1 = \kappa_1 \eta_K$ has been normalized by the Kolmogorov length (which is roughly equal across all simulations), then Figure 3 shows that the motions responsible for turbulent shear stress are shifting to higher wavenumbers at $z^+ = 50$. This shift then allows small particles to more efficiently modify total turbulent transfer.

The shift of cospectra content to higher wavenumbers with increasing Re_b is true both for the uncoupled case (Figure 3(a)) as well as for the particle-laden cases (Figures 3(b)–3(d)). The vertical black lines illustrate the wavenumber at which the integrated cospectra reach 80% of the total turbulent stress $\langle u'w' \rangle$; for the particle-laden cases at a given Re_b , this wavenumber is shifted to the left. If all wavenumbers were affected equally by the presence of the particles, this location would remain unchanged. Instead, while Figure 2 shows that the turbulent flux at nearly all scales

is decreased with the addition of particles (for any Re_b), Figure 3 demonstrates that the decrease is preferentially shifted to high wavenumbers, particularly when $St_K = O(1)$. The shift of momentum flux towards higher wavenumber with increasing Re_b and the resulting preferential damping of high-wavenumber motions by particles partially explains the continued and increasing influence of the dispersed phase with increasing Reynolds number, and in Sec. IV, a detailed analysis of near-wall coherent structures will be used to further explore this effect.

IV. NEAR-WALL COHERENT STRUCTURES

A. Instantaneous structures

Here we use instantaneous fields to gauge the effect of the dispersed phase on near-wall coherent structures. To achieve this, we compute $|\lambda_{ci}|$, the magnitude of the imaginary part of the complex velocity gradient eigenvalue (of the carrier phase) at every grid point throughout the domain. This quantity has been used in previous studies,³⁹ including our own,⁴ to identify regions of swirling motion (or vortices) near the wall. We use the presence of these near-wall coherent motions as evidence of the turbulent flux $\langle u'w' \rangle$.

As a representative example, Figure 4 shows an instantaneous snapshot of surfaces of $|\lambda_{ci}|/(U_0/H) = 2.5$ for both the unladen case and for a laden case with $St_K = O(1)$ at $Re_b = 24000$ (Run 6). Qualitatively, the swirling activity near the wall is reduced by the presence of particles, and the same is generally true for other Reynolds numbers and particle Stokes numbers. The large streaks of blue and red extending across the entire domain in the streamwise direction (prominent in the laden case) show the imprint at the wall of the large-scale rollers. Superimposed on these broad regions are the smaller-scale low- and high-speed streaks which characterize wall-bounded turbulent flows, spaced roughly $\Delta y^+ \approx 100$ apart. Recall that these smaller-scale motions are responsible for the bulk of the turbulent transfer with increasing Re_b as noted in Figures 2 and 3.

Probability density functions (PDFs) of the swirling strength $|\lambda_{ci}|/(U_0/H)$ over the entire domain are plotted in Figure 5. First, it is clear that for the unladen cases, the range of normalized swirling strength increases with Reynolds number, and that beyond a certain strength the PDF has an exponential tail. In this exponential region, the likelihood of finding swirling motions of a given strength decreases significantly with the addition of particles. Furthermore, with increasing $|\lambda_{ci}|$, the gap between the unladen case and each laden case increases significantly (note the ordinate is on a logarithmic scale). As measured by this gap between the unladen and laden probabilities, flows with higher Reynolds numbers experience larger reductions in high-strength swirling motions.

Particles with $St_K = O(1)$ are most effective at reducing the number and strength of the near-wall coherent motions, with the effectiveness reducing as St_K increases. This is true at all Re_b . As discussed in detail in our previous work,⁴ this maximization at $St_K = O(1)$ is due to preferential concentration, which occurs when particles centrifuge out of regions of high vorticity and collect in regions of high strain rate. When the time scale of the particle is on the same order as that of the turbulence (i.e., when $St_K \approx 1$), preferential concentration is maximized.⁴⁰ When the $St_K = O(1)$ particles collect in these regions, local concentrations can be many times higher than the bulk concentration ($\phi_m = 0.25$), and can therefore lead to enhanced turbulence attenuation compared to particles at the same ϕ_m but different St_K .

By contrast, the $St_K = O(10)$ particles cannot respond as quickly to near-surface turbulent motions, and therefore do not collect in the same regions as the $St_K = O(1)$ particles. Instead, their inertial timescale is of the same order as the rotation rate of the Couette rollers,⁴ which causes these more massive particles to collect in the large-scale low-speed streaks (i.e., blue streaks in Figure 4) resulting from the rollers. Thus the influence of $St_K = O(10)$ particles on $|\lambda_{ci}|$ can remain strong, but not with the same efficiency as the $St_K = O(1)$ particles. The $St_K = O(100)$ particles, on the other hand, display almost no preferential concentration and exhibit the least degree of modification to swirling motions within the flow. These differences will be discussed further in Sec. IV B.

Similar to the shear stress spectra of Figure 2, the influence of the particles is not confined to a small range of length or time scales, as Figure 5 illustrates. When the scale separation (i.e., Reynolds number) increases, swirling motions across the entire range of timescales $|\lambda_{ci}|^{-1}$ are influenced; an

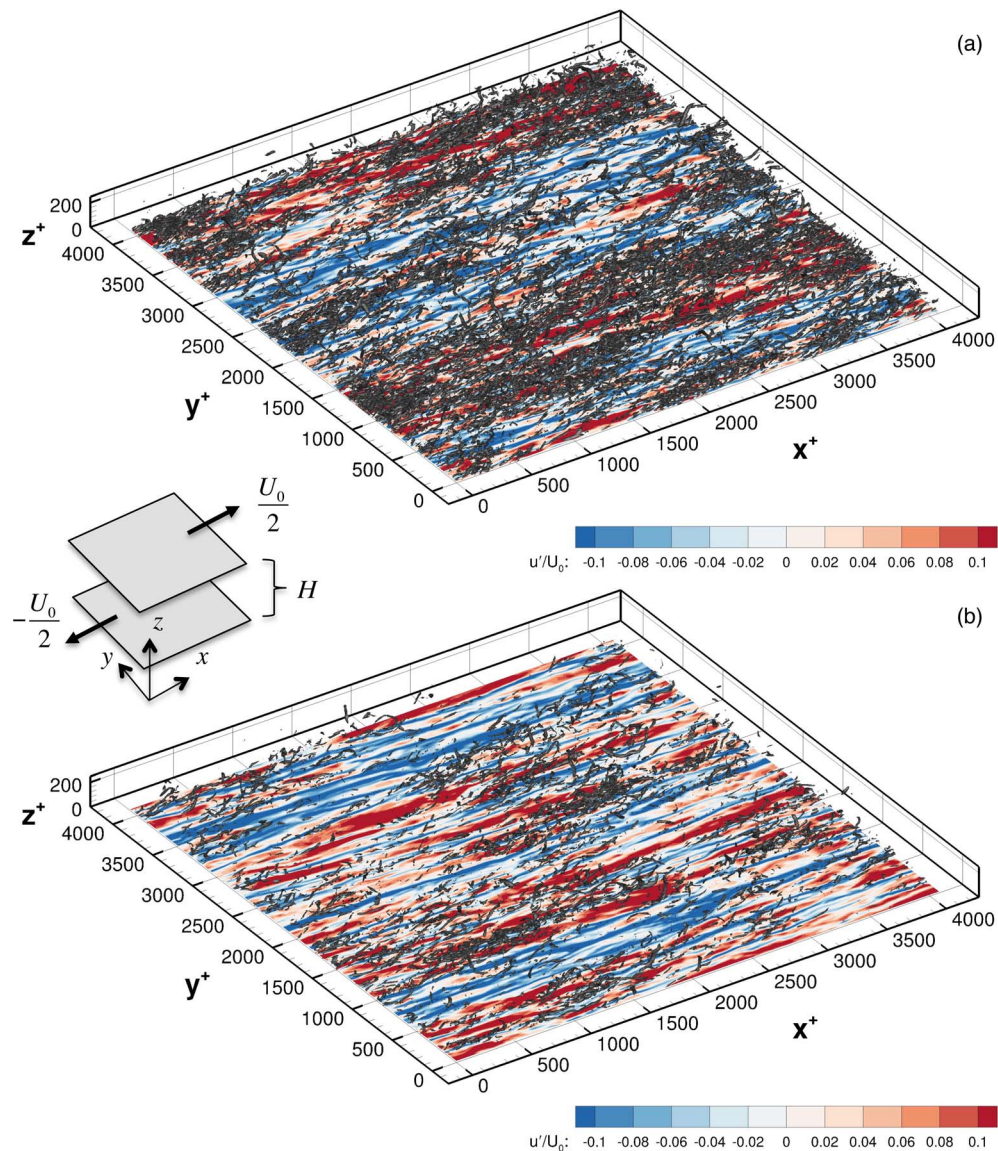


FIG. 4. Instantaneous snapshot for $Re_b = 24000$. Horizontal slice at $z^+ = 15$ shows contours of normalized streamwise velocity fluctuation u'/U_0 and gray structures are iso-surfaces of $|\lambda_{ci}|/(U_0/H) = 2.5$. Compares (a) the unladen case with (b) $St_K = O(1)$. The schematic on the left illustrates the Couette cell layout and coordinate system.

effect which becomes more pronounced with increasing Re_b . We now focus on mechanisms which could lead to this widening of the range of scales over which particles are felt.

B. Conditionally averaged structures

Balachandar and Eaton⁴¹ note in their Sec. 6.2 several mechanisms through which particles can modify turbulence. One is “increased dissipation arising from particle drag,” which for small particles ($d_p/\eta_K \ll 1$) typically results in turbulence attenuation.^{8,42} Previously,⁴ we identified the collective effect of local, particle-scale momentum exchange (i.e., drag on the particle surface) as the primary mechanism through which the dispersed phase damps motions responsible for bulk wall-normal momentum transfer, in agreement with the above quoted mechanism listed by Balachandar and Eaton.⁴¹ This small-scale attenuation of turbulent is evident, for example, in the increase of

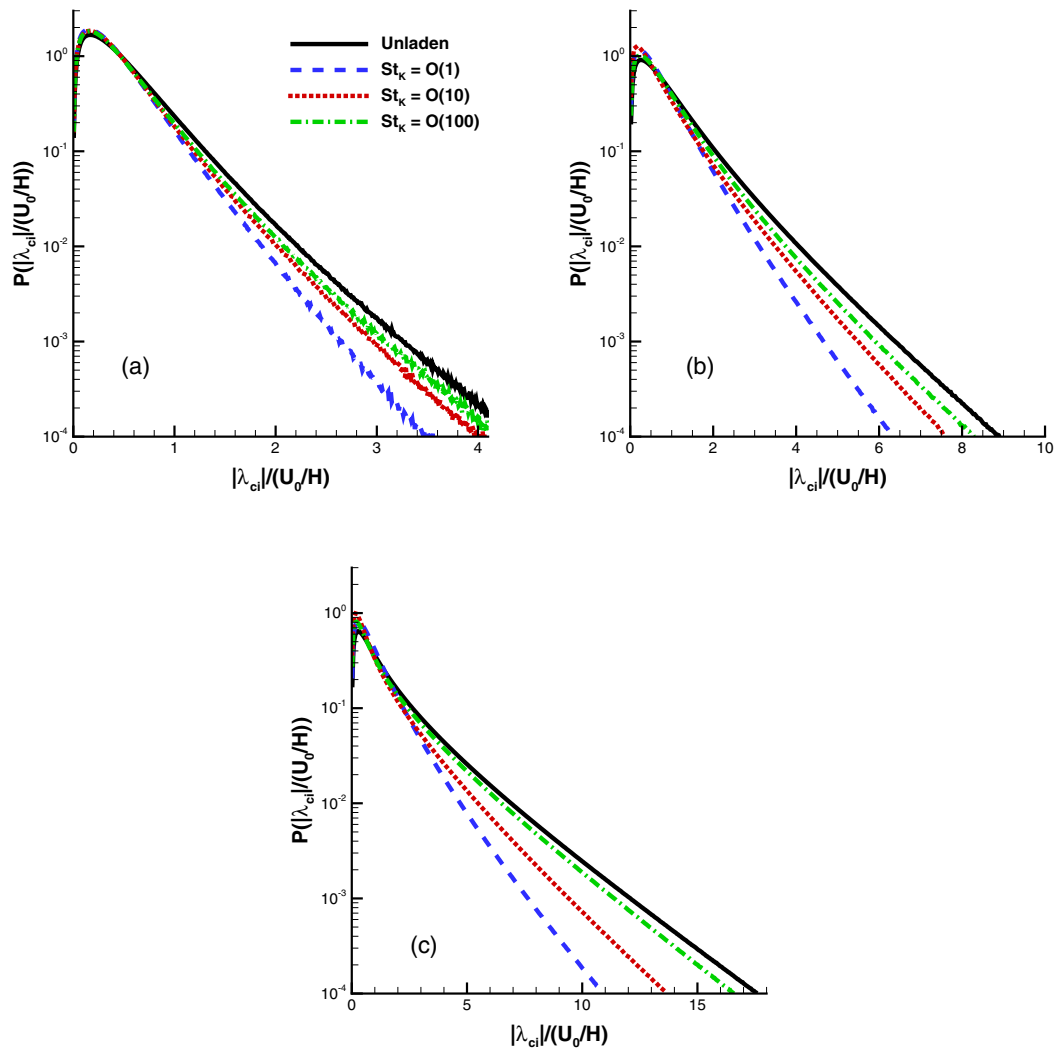


FIG. 5. Probability density function of the normalized swirling strength $|\lambda_{ci}|/(U_0/H)$ for (a) $Re_b = 8100$, (b) $Re_b = 24000$, and (c) $Re_b = 72000$. Each plot contains the probability density function for each particle Stokes number—see legend.

τ_K near the wall after the addition of particles (last column of Table I). At this point, however, we propose an additional mechanism which helps explain the particles' continued influence over an increasingly broad range of scales which exist as Re_b is increased in the current computations. Rather than having the same direct dissipative effect on both large- and small-scale motions, we suggest that by inhibiting the smallest motions near the wall, particles have an up-scale influence which disrupts the formation and evolution of hairpin packets. Individual hairpins have been identified as coherent, near-wall structures which, in an average sense, result in the “bursting” and “sweeping” events that provide the bulk of wall-normal turbulent flux of momentum.⁴³ As they grow and join to form packets, they proliferate throughout a turbulent boundary layer and span length scales ranging up to the boundary layer height.⁴⁴ Their presence has been observed not only in laboratory-scale flows, but in atmospheric-scale flows as well.⁴⁵ In this section, conditional averaging is used to investigate the effects of particles on the hairpin structures which cause these turbulent events.

One method of identifying coherent structures in a turbulent flow, in this case hairpin vortices, is by computing conditionally averaged fields. That is, one constructs an average field based on a specified event of interest at a specified location in the flow. A common approach to identifying the structures associated with near-wall bursting and sweeping events is to define the event using velocity fluctuations corresponding to the second or fourth quadrants of the $u'-w'$ plane.³⁹ We adopt

this procedure for identifying how the presence of particles changes these structures, as well as how this effect changes with Reynolds number. Note that while this procedure can provide details of the flow field conditioned on turbulent sweep and ejection events, it cannot detect changes in the frequency of such events in the flow.

To perform the conditional averaging we use linear stochastic estimation (LSE), a technique which allows computing approximations of conditional averages based on unconditional correlation data.⁴⁶ This is opposed to computing the conditional averages via brute-force, where each sample must be tested against the specified event, which is time-consuming and also results in undersampling depending on the complexity of the event and likelihood of finding such an exact event in the field. LSE has been used in many different applications, particularly in educing coherent structures from turbulent flows, and despite being a linear approximation to the conditional average it has been shown in many cases to be an excellent representation of the true conditional average.⁴⁷

LSE theory is described in detail in other publications,⁴⁶ so only a brief description in the context of the current problem will be provided here. In this description, vectors will be identified either with boldface or index notation when summations are present. Given the event $\mathbf{E}(\mathbf{x}^*, t)$ at event location \mathbf{x}^* , the conditional average of a zero-mean (i.e., fluctuating) quantity \mathbf{y} at location \mathbf{x} is denoted $\langle \mathbf{y} | \mathbf{E} \rangle$. Each element of \mathbf{E} represents a specific event, and the elements of \mathbf{y} are the fields of interest based on the event. In the current study, \mathbf{E} is based on turbulent ejection events near the wall and \mathbf{y} includes the velocity field as well as both the dispersed phase mass concentration field and the dispersed phase feedback force field so that individual hairpins and the corresponding particle feedbacks can be analyzed in detail.

LSE approximates the linearly estimated field $\hat{\mathbf{y}}(\mathbf{x})$ as

$$\hat{y}_i(\mathbf{x}) = L_{ij}(\mathbf{x}, \mathbf{x}^*) E_j(\mathbf{x}^*), \quad (8)$$

where L_{ij} provides, in a least-squares sense, the best linear approximation to the conditional average $\langle \mathbf{y} | \mathbf{E} \rangle$. The rows of L_{ij} must be solved from a linear system which includes unconditional correlations between events:

$$\langle E_j E_l \rangle L_{ij} = \langle y_i E_l \rangle. \quad (9)$$

The conditional field $\hat{\mathbf{y}}$ we are presently concerned with contains velocity fluctuations, the fluctuating particle mass concentration, and the fluctuating feedback forces:

$$\hat{\mathbf{y}}(\mathbf{x}) = [\hat{u}', \hat{v}', \hat{w}', \hat{c}', \hat{F}'_x, \hat{F}'_y, \hat{F}'_z], \quad (10)$$

where F'_i is the fluctuating component of F_i given in Eq. (4) and c' is the fluctuating mass concentration of the dispersed phase. Following previous studies,³⁹ the event $\mathbf{E}(\mathbf{x}^*)$ is chosen as $\mathbf{E} = [u'_m, 0, w'_m]$. Of interest are ejection events, otherwise known as Q2 events, which occur when the streamwise velocity fluctuation u' is negative and the wall-normal velocity fluctuation w' is positive (i.e., ejection of low-momentum fluid away from the wall). The specific event magnitudes u'_m and w'_m are chosen to be those which maximize the contribution to the turbulent flux $\langle u' w' \rangle$ at the specified event height. Mathematically these are the values which lead to the largest product $P(u'_m, w'_m) u'_m w'_m$ where $P(u'_m, w'_m)$ is a joint probability distribution. By setting spanwise velocity fluctuations to zero in \mathbf{E} , we focus only on conditional fields which are spanwise-symmetric.

Figures 6–8 show various conditional fields for the three Reynolds numbers. The event location is $z^+ = 50$. Each figure contains the unladen case (top row), the case when $St_K = O(1)$ (middle row), and the case when $St_K = O(10)$ (bottom row). In all cases, the gray structures represent constant surfaces where the squared swirling strength of the conditional velocity field, $|\lambda_{ci}|^2$, is equal to 15% of the maximum value of the unladen case at the same Reynolds number. For event heights chosen within the range $30 < z^+ < 80$, the conditional structures and their modification due to the addition of particles are very similar at all Reynolds numbers.

Focusing for the moment on the unladen cases (top rows), the contours show conditionally averaged streamwise (left) and wall-normal (right) velocity fluctuations at planes of $z^+ = 8$ and $y^+ = 0$, respectively. The canonical hairpin structure seen in previous channel and boundary-layer flows⁴³ is apparent. Between the counter-rotating legs of the hairpin is an upwelling region of low-

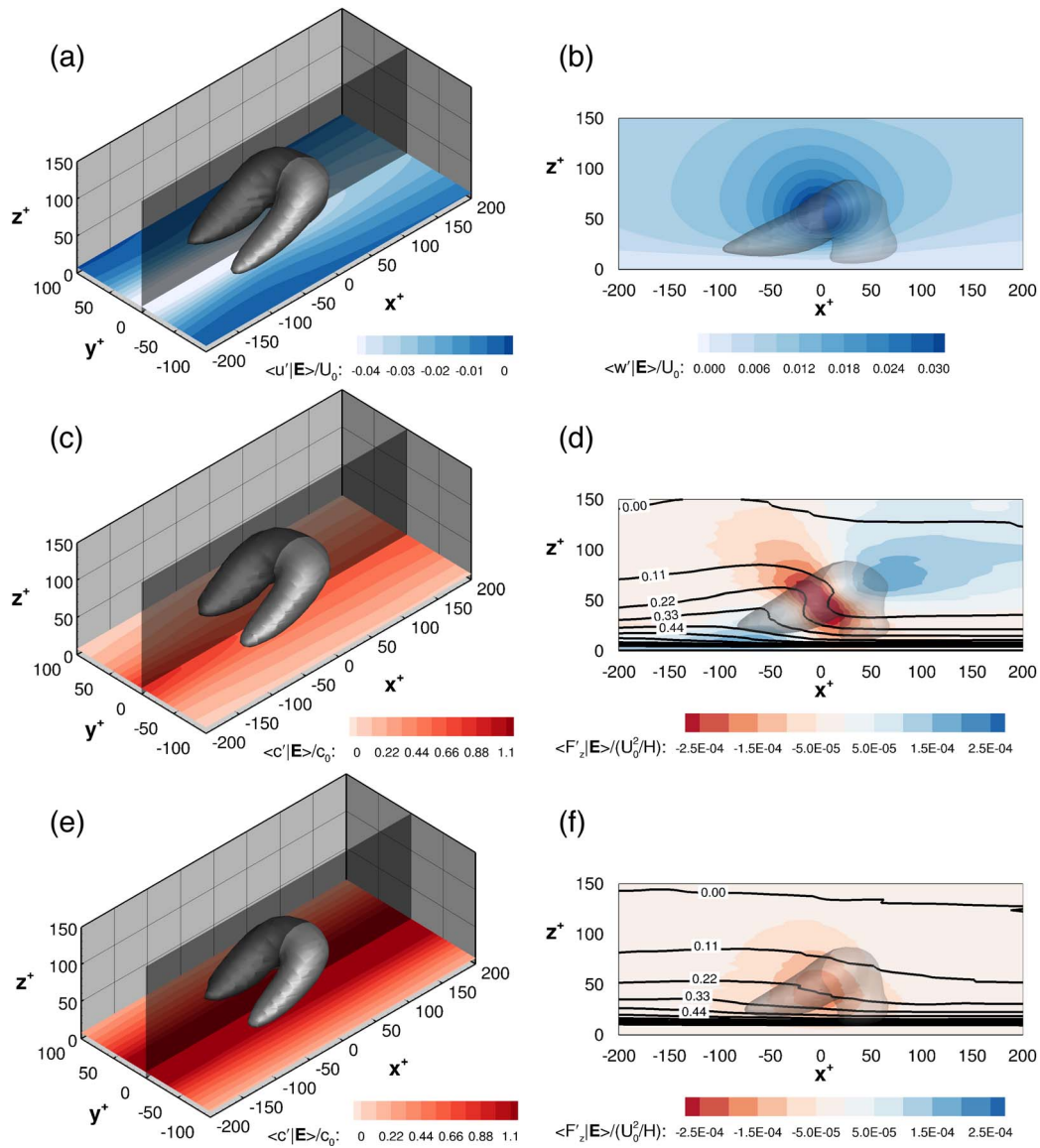


FIG. 6. Conditional structures based on $\mathbf{E} = [u'_m, 0, w'_m]$ for $Re_b = 8100$. Top row corresponds to unladen case, middle row corresponds to $St_K = O(1)$, and bottom row corresponds to $St_K = O(10)$. Horizontal slice in the left column is located at $z^+ = 8$ and the vertical slice in the right column is located at $y^+ = 0$ (denoted as the black, transparent surface in the left column). For the unladen case, the contours represent (a) conditional streamwise velocity fluctuations $\langle u'|\mathbf{E} \rangle / U_0$ and (b) conditional wall-normal velocity fluctuations $\langle w'|\mathbf{E} \rangle / U_0$. For particle laden cases, the solid contours represent (c) and (e) conditional fluctuating concentration $\langle c'|\mathbf{E} \rangle / c_0$ and (d) and (f) conditional particle feedback force in the vertical direction $\langle F'_z|\mathbf{E} \rangle / (U_0^2/H)$. Line contours in (d) and (f) represent levels of conditional particle concentration fluctuations $\langle c'|\mathbf{E} \rangle / c_0$.

velocity fluid, and the fluctuating wall-normal velocity is maximized at the chosen event height. Thus, the Q2-based conditional hairpin is responsible for pulling low-momentum fluid away from the wall and redirecting it upwards, resulting in a negative contribution to the Reynolds stress. With increasing Reynolds number, the shape of the conditional eddy is relatively unchanged, though its streamwise extent is compressed for $Re_b = 72\,000$ when normalized by viscous wall units (consistent with Figure 3).

Figure 6 shows the evolution of the $Re_b = 8100$ conditional eddy as the particle Stokes number increases. In Figures 6(a)–6(f), the horizontal slices (left column) show contours of the conditionally averaged fluctuating particle mass concentration $\langle c'|\mathbf{E} \rangle / c_0$ at $z^+ = 8$ (where c_0 is the bulk con-

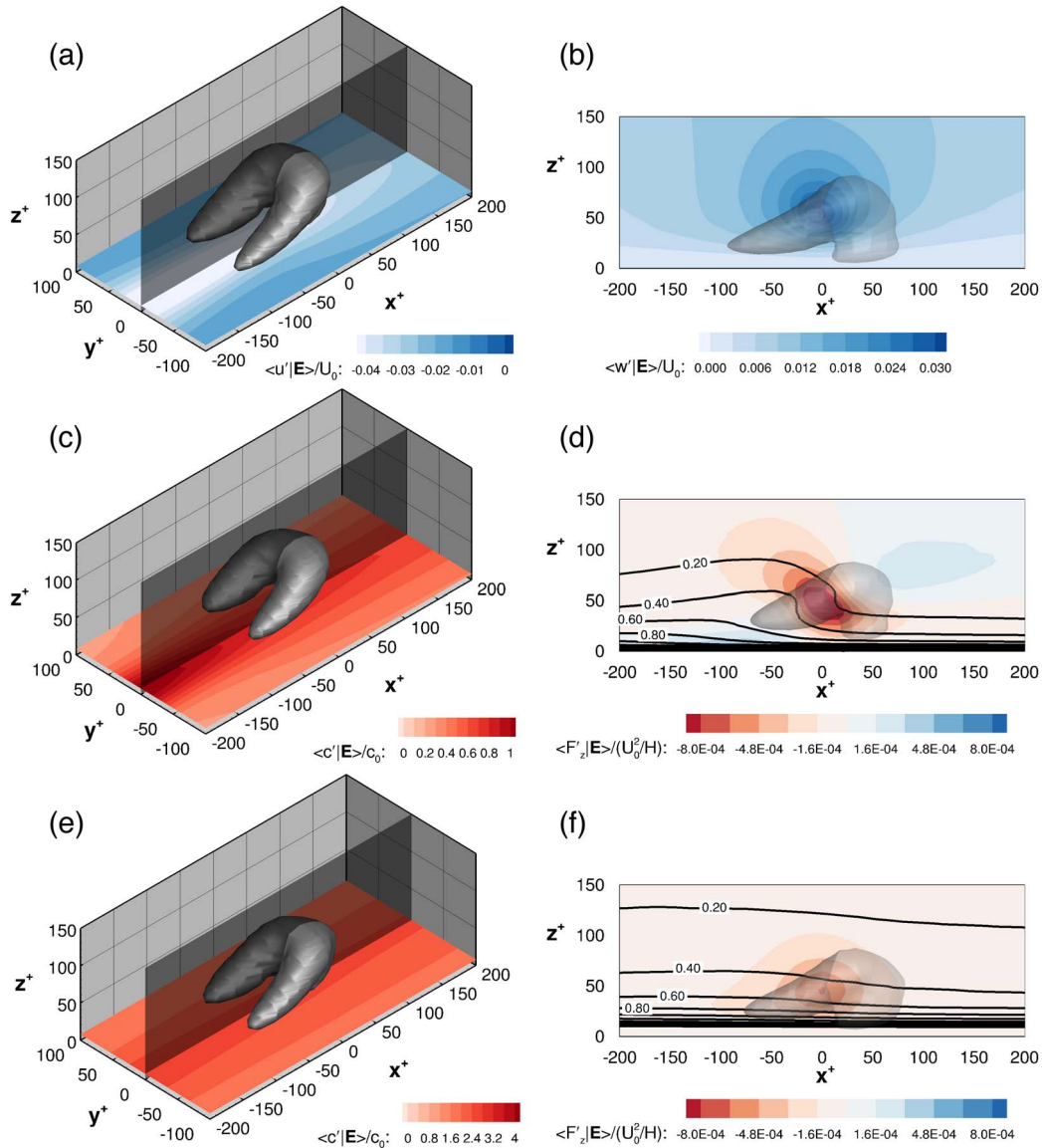
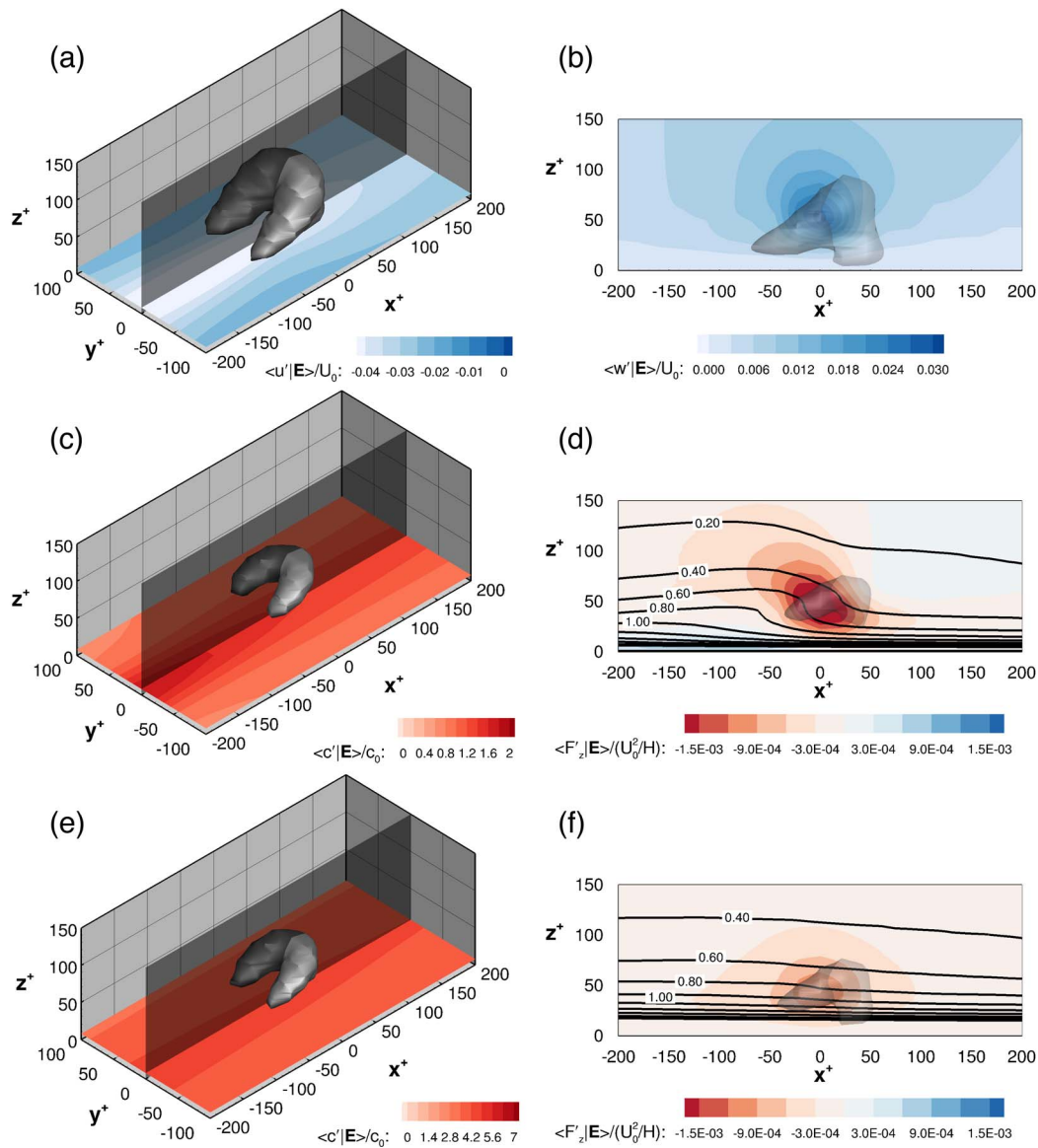


FIG. 7. Same as Figure 6 but for $Re_b = 24\,000$.

centration). In the figures on the right, the slice at $y^+ = 0$ contains contours which illustrate the conditionally averaged vertical force $\langle F'_z | \mathbf{E} \rangle / (U_0^2 / H)$ felt by the fluid due to the dispersed phase, and lines which show contours of $\langle c' | \mathbf{E} \rangle / c_0$.

The figures show that the particle concentration is, on average, higher in the upwelling region between the legs of the hairpin compared to the horizontally averaged concentration. Figure 6(c) shows this clearly for $St_K = O(1)$, where the highest concentrations in the $z^+ = 8$ horizontal plane exist between the legs of the hairpin. In the vertical direction, Figure 6(d) shows that high fluctuating particle concentrations are elevated between the hairpin legs, but upstream of the conditional eddy, where no upwelling occurs, the increased mean particle concentrations do not penetrate upwards. At the event location $[x^+, y^+, z^+] = [0, 0, 50]$, where the wall-normal fluctuations are maximized, the contours in Figure 6(d) show that the dispersed phase pushes down against the vertically directed Q2 event. This resistance to the vertical ejection is largely localized to the region above and below where the hairpin legs meet the head.

FIG. 8. Same as Figure 6 but for $Re_b = 72\,000$.

For $St_K = O(10)$, however, the picture changes dramatically. The distribution of mean particle mass concentration becomes nearly invariant in the x direction. This indicates that the particle organization is no longer primarily due to the near-wall turbulent ejection events. This is consistent with our previous findings,⁴ where particles with $St_K = O(10)$ were found to preferentially concentrate in large regions associated with the large Couette rollers. This is in contrast to the $St_K = O(1)$ particles, which accumulate in smaller-scale regions associated with near-wall streaks, which themselves are signatures of hairpin structures. The vertical distribution of $St_K = O(10)$ particles illustrates the same point: the presence of the conditional eddy only weakly influences the upward movement of dispersed phase mass, as the contour lines are flatter in Figure 6(f) than in Figure 6(d). Since the more inertial particles are unable to collect between the legs of the hairpin as effectively, their mechanical feedback, as measured by their vertical feedback force, is diminished by nearly a factor of 2 when compared to the $St_K = O(1)$ particles.

With increasing Reynolds number, Figures 7 and 8 show that this general behavior remains the same. For an event height of $z^+ = 50$, the $St_K = O(1)$ particles preferentially concentrate in the

region between the hairpin legs, while causing a significant downward force on the carrier phase centered at the location of the ejection event. Once again, more inertial particles ($St_K = O(10)$) are unable to collect on scales associated with the hairpin and therefore result in a lower-magnitude feedback force—a phenomenon which is even stronger at $St_K = O(100)$ (not shown).

V. DISCUSSION

A. Effects of St_K

For the lowest Reynolds number, the effects of the particle Stokes number is described in detail in our previous work.⁴ Each Stokes number probed responds to different timescales within the flow: $St_K = O(1)$ particles have a timescale near the smallest turbulent motions, and thus preferentially concentrate in regions associated with these motions; $St_K = O(10)$ particles have an inertial timescale near the rotation rate of the Couette rollers, and thus preferentially concentrate in the corresponding large-scale convergence regions associated with these motions; and $St_K = O(100)$ particles have an inertial timescale which is larger than any available flow timescale, causing them to maintain a nearly homogeneous concentration throughout a given horizontal slice in the domain.

With increasing Reynolds number, this behavior continues, and the momentum flux modification observed in each case is the end result of the particles' ability to concentrate in regions associated with turbulent ejections and sweeps. Figures 6(c) and 6(d), 7(c) and 7(d), and 8(c) and 8(d) show that $St_K = O(1)$ particles are found to accumulate precisely in regions where they, in being accelerated upwards, provide a force which opposes the motion of the conditional hairpin. The weakened hairpin then cannot vertically transport as much carrier phase momentum through ejection and sweep events.

For $St_K = O(10)$, the picture is slightly more complex since these particles preferentially concentrate in regions associated with the Couette rollers. Figures 6(e) and 6(f), 7(e) and 7(f), and 8(e) and 8(f) show that the conditionally averaged fluctuation field is nearly invariant in the streamwise direction when $St_K = O(10)$. This is in contrast to the $St_K = O(1)$ particles, which show regions of highest concentration only in the vicinity of the hairpin head. This is perhaps most obvious when comparing the contour lines in panels (d) and (f) of Figures 6–8. This streamwise invariance of the $St_K = O(10)$ particle concentration demonstrates that the locations of these particles are not strongly influenced by the relatively small hairpin vortex, which is due to the mismatch in timescales between the hairpin and the particle. At the same time, the conditionally averaged concentration up- and downstream of the hairpin is found to exceed the bulk concentration, implying that the Q2 events tend to occur in regions otherwise occupied by $St_K = O(10)$ particles—the near-wall convergence zones of the Couette rollers (blue streaks in Figure 4). Therefore, while the transport of the $St_K = O(10)$ particles is strongly influenced by the strength and location of the rollers, they do not exhibit the same degree of resistance to Q2 events since they still cannot accumulate in the small-scale regions associated with these motions. Their influence on momentum flux is felt on larger scale-motions in the flow which do not dominate the total momentum transfer (see Figures 2 and 3).

Although not shown for sake of brevity, the hairpins associated with $St_K = O(100)$ motions look qualitatively similar to the unladen cases and no spatial patterns exist for $\langle c'|\mathbf{E} \rangle / c_0$. This indicates that no preferential concentration occurs, and as a result, the peak conditionally averaged feedback force is an order of magnitude smaller than that provided by $St_K = O(1)$ particles.

B. Effects of Re_b

As the Reynolds number increases, the impact which the particles have on the conditional eddies becomes more obvious. At $Re_b = 72\,000$, the strength of the conditional hairpin is diminished substantially, particularly with the addition of particles of $St_K = O(1)$ (as seen in Figure 8(c)). When normalized by channel units, the maximum swirling strength of the conditional eddy increases with Re_b , but is accompanied by a corresponding increase in the resistance force due to the upward ejection of particles.

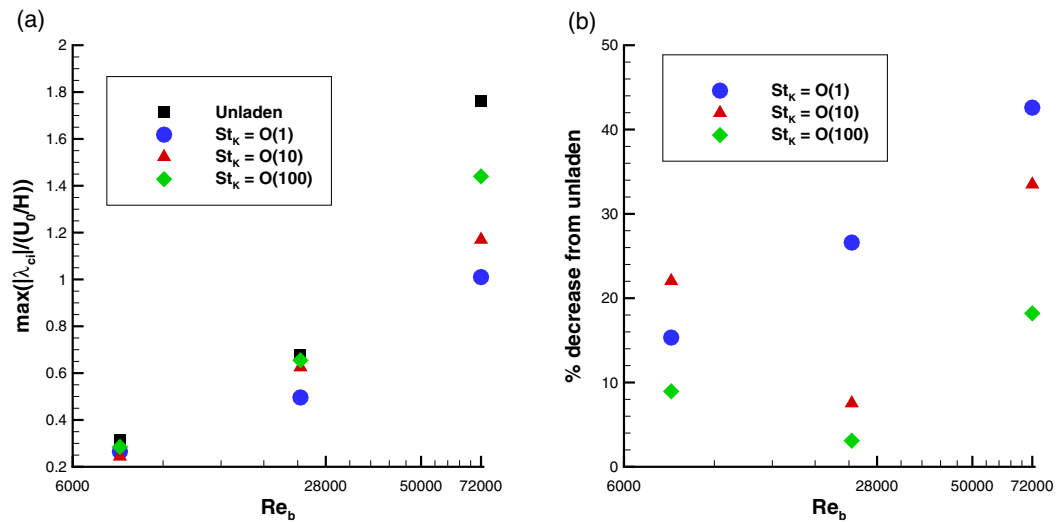


FIG. 9. (a) The maximum normalized swirling strength $\max(|\lambda_{ci}|/(U_0/H))$ of the conditionally averaged velocity field $(\mathbf{u}|\mathbf{E})$ as a function of Re_b . (b) The percent drop of $\max(|\lambda_{ci}|/(U_0/H))$ from the unladen value. Legends contain symbol information. Note that the horizontal axes are on a logarithmic scale.

Figure 9(a) shows the maximum value of $|\lambda_{ci}|$ for each case as a function of Reynolds number. This maximum value of $|\lambda_{ci}|$ is typically located in the curved “head” region of the conditional eddy, and Figure 9(a) clearly shows that the swirling strength in this region is diminished from its unladen value when particles are added. What is surprising is that the capacity of particles to weaken the conditional eddies associated with Q2 events increases significantly with Reynolds number. Figure 9(b) shows the percent reduction of $\max(|\lambda_{ci}|)$ compared to the unladen case for each of the particle Stokes numbers. Reductions in $\max(|\lambda_{ci}|)$ reach nearly 50% for $St_K = O(1)$ at $Re_b = 72\,000$. At all Re_b , the $St_K = O(100)$ particles provide the least resistance to the Q2 motions since they are most unable to preferentially concentrate in the appropriate regions, while at $Re_b \geq 24\,000$ the $St_K = O(1)$ particles provide the highest-magnitude weakening effect.

The ability of particles to weaken the conditional Q2 event is consistent with similar work done by Dritselis and Vlachos^{20,21} in turbulent channel flow, where they find that conditionally averaged quasi-streamwise vortices near the wall are weakened in strength with the presence of inertial particles. Similar to what is seen here, they point out that the particles provide a counter-torque to the rotational sense of their conditional quasi-streamwise vortex, always resisting its rotational motion and thus diminishing its strength. In this sense, the same general phenomenon has also been observed for turbulent wall-bounded flow containing polymer additives. Kim *et al.*⁴⁸ perform a very similar analysis to that presented here, where polymer feedback forces are seen to provide elastic (instead of inertial) resistance to the conditional eddies responsible for Q2 events.

When viewing Figure 9 in light of the behavior of Figures 1 and 2, we see that the effects of the particles are not only influencing scales well separated from their physical size, but that their turbulent-flux-inhibiting behavior increases with Re_b . We therefore speculate that the particles modify the underlying mechanism through which momentum is transferred in wall-bounded turbulence, particularly at high Reynolds number.

Zhou *et al.*³⁹ show in their Figure 11 that only near-wall conditional eddies of sufficient strength can regenerate new hairpin vortices—a mechanism through which coherent turbulent structures multiply and grow throughout the development of near-wall turbulence. If the particles disrupt this regeneration mechanism by damping out the seed structures which initiate the hairpin proliferation process, the particles’ effect will be felt at all scales. In this sense, wall-normal turbulent fluxes in high Reynolds number flows would be impacted more than those in low Reynolds number flow, since the cumulative contribution from the large- and small-scale motions is larger for higher Re . This idea is consistent with the results of Figures 1 and 9.

To provide further evidence of this effect we return to Figure 1, which shows vertical profiles of each component of the stress defined in Eq. (6). Figure 1(a) shows that at $Re_b = 8100$, the decrease in turbulent flux is compensated by an increase in the particle stress. This was discussed in Richter and Sullivan⁴ and illustrates momentum conservation between the carrier and dispersed phases. Momentum transported by turbulent motions is instead transported by individual particles, and the total stress remains nearly constant at all St_K . The same can be said at $Re_b = 24\,000$ (Figure 1(b)), where the turbulent stress decreases across the entire domain height (maximized at $St_K = O(1)$) as discussed previously) but is compensated by an increase in the particle stress. Again this leads to a total stress which does not vary significantly with particle Stokes number. When $Re_b = 72\,000$ (Figure 1(c)), however, the turbulent stress again decreases, but now the increase in particle stress does not completely compensate for this loss. Instead, the total stress decreases, indicating that the total amount of momentum being transferred across the Couette cell is now less than that for the unladen case.

At lower Re_b , the overall behavior can be described as momentum conservation between the phases, where the damping of turbulent fluctuations by individual particles translates into momentum gained by the dispersed phase. The separation between the largest and smallest scales is small, so particles directly interact and exchange momentum with nearly all scales which are available in the flow. At high Re_b , however, this simple explanation does not hold. Our proposed mechanism would suggest that at higher Re_b , the particles continue to exchange momentum with motions at their immediate spatial scales (i.e., the smallest motions of turbulence), but that this interaction inhibits larger structures from ever forming, manifesting itself as a decrease in the total stress across the system. This is enhanced by the fact that the scales associated with the turbulent flux shift to high wavenumbers with increases in Re_b (cf. Figure 3). The process by which particles disrupt hairpin regeneration also explains the behavior in Figures 2 and 5, where the dispersed phase alters motions well beyond their spatial and temporal time scales. Therefore as the Reynolds number approaches the truly “high” limit (e.g., geophysical flows), where the energy spectra and shear stress cospectra become independent of Re_b at scales corresponding to the inertial subrange and below, we speculate that the influence of particles would continue to be felt since the turbulence cascade and the motions responsible for it have been modified.

VI. CONCLUSIONS

The ability of particles to influence momentum transfer in turbulent Couette flow, particularly as the Reynolds number is increased, is studied using a combination of DNS and Lagrangian point-particle tracking. Our previous work⁴ shows that inertial particles reduce near-wall swirling motions, which in turn results in a reduction of the turbulent Reynolds stress. Here, we perform conditional averaging via linear stochastic estimation⁴⁶ to better understand the physical mechanisms responsible for the observed reduction in turbulent momentum flux with the addition of particles. Several key observations are made:

1. The number and strength of instantaneous near-wall swirling motions, as measured by $|\lambda_{ci}|$, is diminished significantly with the addition of particles.
2. Particles whose Stokes numbers are $O(1)$ are most able to preferentially concentrate on scales associated with the conditional hairpin structures corresponding to a Q2 event. These $St_K = O(1)$ particles therefore result in the largest feedback force between the carrier and dispersed phases, opposing the ejection motion caused by the conditional eddy and weakening the eddy strength.
3. With increasing Reynolds number, the particle influence on the conditional hairpin strength increases, as measured by the deviation from the unladen conditional eddy strength. Again, $St_K = O(1)$ particles exhibit the largest effect.

We therefore propose that particles, despite interacting with the carrier phase on scales on the order of their diameter (which is assumed smaller than the Kolmogorov length), can influence turbulent transport at scales much larger than their size by disrupting the regeneration process of near-wall turbulent motions—a process made more efficient by the concentration of flux-producing

scales towards high wavenumbers observed with increasing Reynolds number. Furthermore, this proposed mechanism highlights a need for better understanding the direct, two-way interaction between turbulent motions and particle clusters (which can exist at multiple spatial scales, unlike individual particles). This interaction remains a current target of continuing analysis.

ACKNOWLEDGMENTS

The authors are grateful for the Accelerated Scientific Discovery computer allocation at the National Center for Atmospheric Research, through which the simulations were run. We would like to acknowledge high-performance computing support from the Yellowstone system provided by NCAR's Computational and Information Systems Laboratory. The authors would also like to thank the Advanced Study Program for financial support. The National Center for Atmospheric Research is supported by the National Science Foundation.

- ¹P. R. Owen, "Pneumatic transport," *J. Fluid Mech.* **39**(02), 407–432 (1969).
- ²Mariano I. Cantero, Mrugesh Shringarpure, and S. Balachandar, "Towards a universal criteria for turbulence suppression in dilute turbidity currents with non-cohesive sediments," *Geophys. Res. Lett.* **39**, L14603 doi:10.1029/2012GL052514 (2012).
- ³Raymond A. Shaw, "Particle-turbulence interactions in atmospheric clouds," *Annu. Rev. Fluid Mech.* **35**, 183–227 (2003).
- ⁴David H. Richter and Peter P. Sullivan, "Momentum transfer in a turbulent, particle-laden Couette flow," *Phys. Fluids* **25**, 053304 (2013).
- ⁵David H. Richter and Peter P. Sullivan, "Sea surface drag and the role of spray," *Geophys. Res. Lett.* **40**, 656–660 doi:10.1002/grl.50163 (2013).
- ⁶David H. Richter and Peter P. Sullivan, "The sea spray contribution to sensible heat flux," *J. Atmos. Sci.* **71**(2), 640–654 (2014).
- ⁷Jonathan D. Kulick, John R. Fessler, and John K. Eaton, "Particle response and turbulence modification in fully developed channel flow," *J. Fluid Mech.* **277**, 109–134 (1994).
- ⁸Tomohiko Tanaka and John K. Eaton, "Classification of turbulence modification by dispersed spheres using a novel dimensionless number," *Phys. Rev. Lett.* **101**, 114502 (2008).
- ⁹Yutaka Tsuji, Yoshinobu Morikawa, and Hiroshi Shiomi, "LDV measurements of an air-solid two-phase flow in a vertical pipe," *J. Fluid Mech.* **139**, 417–434 (1984).
- ¹⁰Yiming Li, John B. McLaughlin, K. Kontomaris, and L. Portela, "Numerical simulation of particle-laden turbulent channel flow," *Phys. Fluids* **13**(10), 2957–2967 (2001).
- ¹¹M. Rashidi, G. Hetsroni, and Sanjoy Banerjee, "Particle-turbulence interaction in a boundary layer," *Int. J. Multiphase Flow* **16**(6), 935–949 (1990).
- ¹²M. Righetti and G. P. Romano, "Particle-fluid interactions in a plane near-wall turbulent flow," *J. Fluid Mech.* **505**, 93–121 (2004).
- ¹³Bert Vreman, Bernard J. Geurts, N. G. Deen, J. A. M. Kuipers, and J. G. M. Kuerten, "Two- and four-way coupled Euler–Lagrangian large-eddy simulation of turbulent particle-laden channel flow," *Flow, Turbul. Combust.* **82**, 47–71 (2008).
- ¹⁴P. Gualtieri, F. Picano, G. Sardina, and C. M. Casciola, "Clustering and turbulence modulation in particle-laden shear flows," *J. Fluid Mech.* **715**, 134–162 (2013).
- ¹⁵Lihao Zhao, Helge I. Andersson, and J. J. J. Gillissen, "Turbulence modulation and drag reduction by spherical particles," *Phys. Fluids* **22**, 081702 (2010).
- ¹⁶Yoichi Mito and Thomas J. Hanratty, "Effect of feedback and inter-particle collisions in an idealized gas-liquid annular flow," *Int. J. Multiphase Flow* **32**, 692–716 (2006).
- ¹⁷A. W. Vreman, "Turbulence characteristics of particle-laden pipe flow," *J. Fluid Mech.* **584**, 235–279 (2007).
- ¹⁸N. Caraman, J. Borée, and Olivier Simonin, "Effect of collisions on the dispersed phase fluctuation in a dilute tube flow: Experimental and theoretical analysis," *Phys. Fluids* **15**, 3602 (2003).
- ¹⁹J. Borée and N. Caraman, "Dilute bidispersed tube flow: Role of interclass collisions at increased loadings," *Phys. Fluids* **17**, 055108 (2005).
- ²⁰Chris D. Dritselis and Nicholas S. Vlachos, "Numerical study of educed coherent structures in the near-wall region of a particle-laden channel flow," *Phys. Fluids* **20**, 055103 (2008).
- ²¹Chris D. Dritselis and Nicholas S. Vlachos, "Numerical investigation of momentum exchange between particles and coherent structures in low Re turbulent channel flow," *Phys. Fluids* **23**, 025103 (2011).
- ²²Lihao Zhao, Helge I. Andersson, and Jurriaan J. J. Gillissen, "Interphasial energy transfer and particle dissipation in particle-laden wall turbulence," *J. Fluid Mech.* **715**, 32–59 (2013).
- ²³S. Tenneti and S. Subramaniam, "Particle-resolved direct numerical simulation for gas-solid flow model development," *Annu. Rev. Fluid Mech.* **46**, 199–230 (2014).
- ²⁴R. Clift, John R. Grace, and Martin E. Weber, *Bubbles, Drops, and Particles* (Academic Press, 1978).
- ²⁵Martin R. Maxey and James J. Riley, "Equation of motion for a small rigid sphere in nonuniform flow," *Phys. Fluids* **26**(4), 883–889 (1983).
- ²⁶M. Boivin, O. Simonin, and Kyle D. Squires, "On the prediction of gas–solid flows with two-way coupling using large eddy simulation," *Phys. Fluids* **12**(8), 2080–2090 (2000).

- ²⁷ R. S. Miller and J. Bellan, "Direct numerical simulation of a confined three-dimensional gas mixing layer with one evaporating hydrocarbon-droplet-laden stream," *J. Fluid Mech.* **384**, 293–338 (1999).
- ²⁸ J. Komminaho, A. Lundbladh, and Arne V. Johansson, "Very large structures in plane turbulent Couette flow," *J. Fluid Mech.* **320**, 259–285 (1996).
- ²⁹ T. Tsukahara, H. Kawamura, and K. Shingai, "DNS of turbulent Couette flow with emphasis on the large-scale structure in the core region," *J. Turbul.* **7**(19), N19 (2006).
- ³⁰ Philippe R. Spalart, Robert D. Moser, and Michael M. Rogers, "Spectral methods for the Navier-Stokes equations with one infinite and two periodic directions," *J. Comput. Phys.* **96**, 297–324 (1991).
- ³¹ B. P. K. Yung, H. Merry, and T. R. Bott, "The role of turbulent bursts in particle re-entrainment in aqueous systems," *Chem. Eng. Sci.* **44**(4), 873–882 (1989).
- ³² J. O. Hinze, "Fundamentals of the hydrodynamic mechanism of splitting in dispersion processes," *AIChE J.* **1**(3), 289–295 (1955).
- ³³ Y. Yamamoto, M. Potthoff, T. Tanaka, T. Kajishima, and Yutaka Tsuji, "Large-eddy simulation of turbulent gas-particle flow in a vertical channel: Effect of considering inter-particle collisions," *J. Fluid Mech.* **442**, 303–334 (2001).
- ³⁴ H. Schlichting, *Boundary-Layer Theory*, 6th ed. (McGraw-Hill, 1968).
- ³⁵ K. Hadinoto, E. N. Jones, C. Yurteri, and J. S. Curtis, "Reynolds number dependence of gas-phase turbulence in gas-particle flows," *Int. J. Multiphase Flow* **31**, 416–434 (2005).
- ³⁶ C. Poelma and G. Ooms, "Particle-turbulence interaction in a homogeneous, isotropic turbulent suspension," *Appl. Mech. Rev.* **59**(2), 78–90 (2006).
- ³⁷ Thomas H. van den Berg, S. Luther, and D. Lohse, "Energy spectra in microbubbly turbulence," *Phys. Fluids* **18**, 038103 (2006).
- ³⁸ D. Molin, C. Marchioli, and A. Soldati, "Turbulence modulation and microbubble dynamics in vertical channel flow," *Int. J. Multiphase Flow* **42**, 80–95 (2012).
- ³⁹ J. Zhou, Ronald J. Adrian, S. Balachandar, and T. M. Kendall, "Mechanisms for generating coherent packets of hairpin vortices in channel flow," *J. Fluid Mech.* **387**, 353–396 (1999).
- ⁴⁰ Damian W. I. Rouson and John K. Eaton, "On the preferential concentration of solid particles in turbulent channel flow," *J. Fluid Mech.* **428**, 149–169 (2001).
- ⁴¹ S. Balachandar and John K. Eaton, "Turbulent dispersed multiphase flow," *Annu. Rev. Fluid Mech.* **42**, 111–133 (2010).
- ⁴² R. A. Gore and Clayton T. Crowe, "Effect of particle size on modulating turbulent intensity," *Int. J. Multiphase Flow* **15**(2), 279–285 (1989).
- ⁴³ Ronald J. Adrian, "Hairpin vortex organization in wall turbulence," *Phys. Fluids* **19**, 041301 (2007).
- ⁴⁴ K. T. Christensen and Ronald J. Adrian, "Statistical evidence of hairpin vortex packets in wall turbulence," *J. Fluid Mech.* **431**, 433–443 (2001).
- ⁴⁵ Scott E. Himmema and Ronald J. Adrian, "Packet structure of surface eddies in the atmospheric boundary layer," *Boundary-Layer Meteorol.* **106**(1), 147–170 (2003).
- ⁴⁶ Ronald J. Adrian, "Stochastic estimation of the structure of turbulent fields," in *Eddy Structure Identification*, edited by J. P. Bonnet (Springer, 1996), pp. 145–195.
- ⁴⁷ Ronald J. Adrian, B. G. Jones, M. K. Chung, Yassin Hassan, C. K. Nithianandan, and A. T.-C. Tung, "Approximation of turbulent conditional averages by stochastic estimation," *Phys. Fluids A* **1**(6), 992–998 (1989).
- ⁴⁸ Kyoungyoun Kim, Chang-F. Li, R. Sureshkumar, S. Balachandar, and Ronald J. Adrian, "Effects of polymer stresses on eddy structures in drag-reduced turbulent channel flow," *J. Fluid Mech.* **584**, 281 (2007).